

Physical properties and the variability mechanism of the He I outflow in NGC 4151

C. Wildy^{1*}, H. Landt^{2†}, M. R. Goad¹, M. Ward^{2†} and J. S. Collinson²

¹*University of Leicester, Department of Physics and Astronomy, University Road, Leicester, UK*

²*Department of Physics, Durham University, South Road, Durham DH1 3LE, UK*

Received xxx; in original form January 0000

ABSTRACT

We report on variable helium absorption lines in NGC 4151 observed across six epochs of quasi-simultaneous near-infrared and optical data. These observations cover the transitions from the metastable 2^3S state at 3889 Å and 10830 Å, and from the 2^1S state at 20587 Å. This is the first AGN absorption line variability study to include measurements of the 20587 Å line. The physical properties of the absorber recorded at the fifth observational epoch are relatively well constrained by the presence of absorption in both the optical and near-infrared components, with the 10830 Å line likely saturated. The observations suggest variations in this absorber’s strength are best explained by ionization changes in response to a variable incident continuum. Photoionization simulations constrain the total hydrogen number density of the epoch 5 absorber to $7.1 \leq \log(n_{\text{H}}/\text{cm}^{-3}) \leq 8.8$, the hydrogen column density to $21.2 \leq \log(N_{\text{H}}/\text{cm}^{-2}) \leq 23.3$ and the ionization parameter range to $-1.9 \leq \log U \leq 0.4$. The simulations also suggest the absorber is located between 0.03 and 0.49 pc from the continuum emission region. This range in physical properties is consistent with an absorber of similar velocity seen in NGC 4151 from previous ultraviolet and optical studies, but with high column density X-ray absorbing components not present. The mass outflow rate due to the fifth epoch absorber is in the range 0.008 to $0.38 M_{\odot} \text{ yr}^{-1}$, too low to contribute to galaxy feedback effects.

Key words: AGN absorption/emission lines – optical: AGN.

1 INTRODUCTION

Outflows from Active Galactic Nuclei (AGN) can be manifested by blueshifted absorption lines and are detected in wavelength bands ranging from X-rays to the near-infrared (hereafter, near-IR). These outflows can attain velocities of up to 20 per cent of the vacuum light speed in the host galaxy rest-frame (Pounds et al. 2003), and may be accelerated by radiation pressure, magnetic effects or thermal expansion (Chelouche & Netzer 2001; Everett 2005; Giustini & Proga 2012). Outflows are thought to have a significant impact on the host galaxy and may regulate black growth via feedback (Magorrian et al. 1998; Silk & Rees 1998; Scannapieco & Oh 2004; Wang et al.

2006; Nardini et al. 2015). Many absorption features in AGN are observed to undergo variability across a wide range of timescales spanning hours to several years (Risaliti 2010; Filiz Ak et al. 2013). The mechanism responsible for this variability is suggested to be either movement of gas across the line-of-sight or changes in its ionization state (Arav 1998; Hamann et al. 2008).

The Seyfert 1 Galaxy NGC 4151 has undergone intensive study across the electromagnetic spectrum since it hosts one of the closest and brightest active nuclei as seen from Earth. One of its most intriguing characteristics is the dramatic variability in the strength of the continuum emission, a phenomenon which is observed in X-ray, ultraviolet (UV) and optical wavebands (Edelson et al. 1996). The spectral variability of the absorption lines has, however, been less intensively studied. An investigation of the narrow line region (NLR) in NGC 4151 has revealed a possible geometry for the outflowing gas, indicating that it originates in a conical region with a full opening angle of $\sim 80^\circ$ with a line-of-sight viewing angle lying 10° outside of the cone (Hutchings et al. 1998).

* E-mail: cw268@le.ac.uk

† Visiting Astronomer at the Infrared Telescope Facility, which is operated by the University of Hawaii under Cooperative Agreement no. NNX-08AE38A with the National Aeronautics and Space Administration, Science Mission Directorate, Planetary Astronomy Program.

Optical spectroscopic observations obtained using the Space Telescope Imaging Spectrograph (STIS) aboard the Hubble Space Telescope (HST) indicated that Balmer and metastable helium absorption features, which had previously only been observed during low continuum states, were also present during high continuum states. They also measured higher outflow velocities at higher continuum fluxes (Hutchings et al. 2002). A series of papers (Crenshaw et al. 2000; Kraemer et al. 2001, 2005, 2006; Crenshaw & Kraemer 2007) reported that the absorption features seen in the UV and optical transitions across a range of ionization states were dominated by a feature labelled “D+E”. This feature had a radial velocity centroid of $\approx -500 \text{ km s}^{-1}$ relative to the rest-frame of the source with a full-width at half-maximum (FWHM) of 1170 km s^{-1} . The absorbing material was found to be located at a distance of $\sim 0.1 \text{ pc}$ from the central engine with a number density of between 10^7 and 10^9 cm^{-3} .

A situation frequently encountered when analysing AGN absorption lines is that of saturation at non-zero residual intensities. A signature of this effect is when two components of an absorber have an observed ratio of line optical depths closer to 1:1 than that which atomic theory predicts, implying the stronger component has reached opacity over at least part of its wavelength span. This is especially noticeable in many UV absorbers having doublet structures such as Si IV $\lambda\lambda 1394, 1403$ and C IV $\lambda\lambda 1548, 1551$ where the predicted optical depth ratio is 2:1. In these cases the effect is interpreted as resulting from an absorber which only partially covers the emission region (Arav 1998). This can pose a problem for accurate determination of the outflow column densities since the uncertainty in the predicted column density becomes large as doublet component ratios approach unity.

A solution to the problem of saturated doublet components is to observe lines with large theoretical optical depth ratios, ensuring that, even at high column densities, the apparent optical depth ratio remains large. An excellent candidate for this kind of study is absorption arising from the $n=2$ triplet state metastable level in the helium atom. This excited state has an average lifetime of ~ 2.2 hours (Drake 1971) and is 19.8 eV above the ground state, ensuring that it is predominately populated through recombination of He II, rather than collisional excitation. As a result, the absorption lines from this level in the optical to near-IR range occurring at 3889 \AA and 10830 \AA are effectively high-ionization transitions. For AGN at higher redshift, a particular advantage of the study of these lines is that they are not contaminated by Ly α forest absorption. This contrasts with the use of P V $\lambda\lambda 1118, 1128$ as a high ionization, high column density-sensitive absorber, whose wavelength is blueward of the Ly α line. The He I singlet level 2^1S can also be considered metastable, although its lifetime, at ~ 0.11 seconds, is considerably shorter than that of the 2^3S level.

The usefulness of metastable helium in AGN absorption line research was demonstrated by Leighly et al. (2011), in which the first example of a He I $\lambda 10830$ broad absorption line quasar was analysed and from which the outflow properties were constrained. Their investigation used two of the triplet components present in the near-IR at 10830 \AA and optical at 3889 \AA , which have a theoretical optical depth ratio of 23.3:1. A third absorption line representing a transition

from the triplet metastable state can be found at 3188 \AA . However, this transition is outside of the optical data’s spectral range given the low redshift of NGC 4151. Recent studies of AGN metastable helium absorption are also described in Ji et al. (2015) and Liu et al. (2015). The transition from the He I singlet state due to absorption of 20587 \AA photons can also appear as a weak blueshifted feature. This absorber is not well studied in the literature, however a detection was reported in the near-IR spectrum of NGC 4151 by Iserlohe et al. (2013) (See §7.2 and fig. 9 in that paper).

This paper investigates the absorption lines resulting from the triplet state absorption components at 3889 \AA and 10830 \AA as well as that due to the transition from the singlet state at 20587 \AA in an attempt to identify the variability mechanism and constrain the absorber properties. To our knowledge the work described here is the first to examine an AGN outflow using absorption features from all three of the above transitions. This paper is structured as follows: (a) §2 describes the observations taken, (b) §3.1 and §3.2 describe in detail the procedure used to construct the unabsorbed models from which absorption strength is measured, (c) §3.3 details the calculation of column densities, (d) §4 describes the photoionization simulations used, and (e) §5 provides conclusions derived from the observations/simulations.

2 NEAR-IR AND OPTICAL SPECTROSCOPY

We are using here six epochs of quasi-simultaneous (within 37 days) near-IR and optical spectroscopy for NGC 4151 (see Table 1). The near-IR spectroscopy was obtained using the SpeX spectrograph (Rayner et al. 2003) at the NASA Infrared Telescope Facility (IRTF), a 3m telescope on Mauna Kea, Hawai’i, in the short cross-dispersed mode (SXD, $0.8 - 2.4 \mu\text{m}$). All data except those from 2010 were obtained through a slit of $0.8 \times 15''$ giving an average spectral resolution of full width at half maximum (FWHM) $\sim 400 \text{ km s}^{-1}$. A narrower slit of $0.3 \times 15''$ was used for the 2010 epoch. The three epochs spanning the years 2004 – 2007 were presented in Landt et al. (2011), with the 2004 observation also discussed in Landt et al. (2008). The near-IR spectra from 2002 and 2010 were discussed by Riffel et al. (2006) and Schnülle et al. (2013), respectively. The recent near-IR spectrum from 2015 was obtained with the refurbished SpeX as part of a variability campaign and will be discussed in detail elsewhere (Landt et al., in prep.).

The optical spectra, with the exception of the most recent one, were obtained with the FAST spectrograph (Fabricant et al. 1998) at the Tillinghast 1.5 m telescope on Mt. Hopkins, Arizona, using the 300 l/mm grating and a long-slit of $3''$ aperture. This set-up resulted in a wavelength coverage of $\sim 3720 - 7515 \text{ \AA}$ and an average spectral resolution of FWHM $\sim 330 \text{ km s}^{-1}$. Except for the 2004 data, all spectra were observed at a very low airmass (sec $z \sim 1.05$). The May 2004 spectrum was observed at an airmass of sec $z \sim 1.3$ and so the flux loss due to atmospheric differential refraction is expected to be $\sim 20\%$ at the observed wavelength of He I $\lambda 3888$ relative to that at wavelengths $\geq 5000 \text{ \AA}$ (Filippenko 1982). All FAST optical spectra were retrieved from the FAST archive. The optical spectrum from 2015 was obtained with the ISIS dual-arm spectrograph at the William Herschel 4.2 m telescope on La

Palma, Canary Islands, using the 600 l/mm and 316 l/mm gratings for the blue and red arm, respectively, and a 1'' aperture long-slit. This set-up resulted in a total wavelength coverage of $\sim 3690 - 8800 \text{ \AA}$ and an average spectral resolution of $\text{FWHM} \sim 75 \text{ km s}^{-1}$ and $\sim 145 \text{ km s}^{-1}$ in the blue and red arm, respectively. The spectrograph slit was rotated to align with the parallactic angle, in order to minimise the effect of atmospheric refraction on the analysis. Reduction of the optical data was performed within IRAF, while the IRTF reduction was carried out using *Spec-tool* (Cushing et al. 2004). Before any analysis of the data was performed, all spectra were adjusted to the object rest-frame.

3 ANALYSIS

3.1 Spectral adjustments

The six spectra were observed at optical and near-IR wavelengths in order to span the 2^3S He I emission and absorption features resulting from two of the components, at 3889 \AA and 10830 \AA . In both wavebands small additive wavelength shifts were made to account for differences in wavelength calibration across the various epochs by aligning the spectra to the wavelengths of strong skylines prior to correction for redshift. Before any analysis of the spectra were undertaken, small variations in the effective resolution were removed by identifying the spectrum across both sets of observations with the broadest narrow features. All other spectra were then convolved with a Gaussian of unit area and appropriate FWHM to match the resolution of this spectrum ($\sim 400 \text{ km s}^{-1}$) while preserving the area of emission and absorption features.

3.2 The unabsorbed spectrum

Reconstruction of the unabsorbed spectrum is required in order to measure the depth of the absorption features. This process is complicated by the overlap of emission from several different sources, namely the AGN power-law continuum, the broad line region (BLR) including a continuum of blended broad Fe II emission, the NLR, the torus and the host galaxy. To deal with the relatively featureless and continuous aspects of this emission, the aforementioned Fe II continuum together with the host galaxy starlight and AGN power-law contributions were fitted simultaneously to the same relatively line-free regions of the spectra at each epoch using the IRAF *specfit* package, which was also used in all subsequent spectral fitting described in this paper. For the near-IR spectra, an additional contribution from the dusty torus was modelled using a blackbody. The Fe II model was scaled from the template obtained from I Zw 1 by Véron-Cetty et al. (2004), which was also Gaussian-blurred to approximate the width of the broad emission lines in the spectrum. The host galaxy contribution was built from the Sa and Sb-type spiral galaxy templates listed in the SWIRE library (Polletta et al. 2007). Epochs 2, 3 and 4 have estimated galaxy fluxes, derived from HST observations, listed in Landt et al. (2011). Galaxy templates were therefore normalised to match these fluxes prior to running the *specfit* fitting routine, minimising the problem of degenerate fitting.

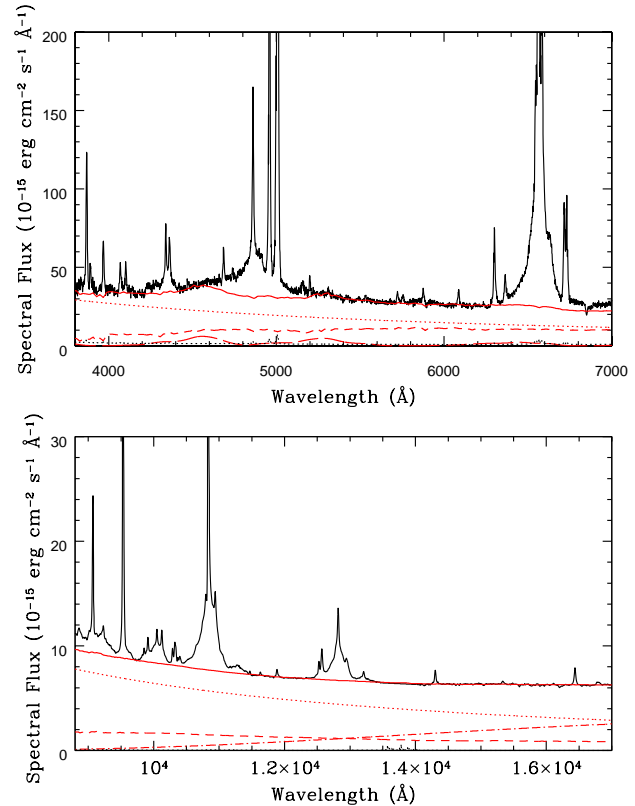


Figure 1. Continuous emission fits to the optical spectrum (top panel) and the near-IR spectrum (bottom panel) at epoch 1. The AGN continuum (red dotted line), host galaxy (red short-dashed line), Fe II broad emission (red long-dashed line) and blackbody torus emission (red dot-dashed line) are indicated along with the observed spectrum and its associated error spectrum (black solid and black dotted lines respectively). The total continuous emission model is indicated by the red solid line. The near-IR errors are barely visible due to the high S/N.

Epochs without such observations used an average value, corrected when necessary for differences in slit width. An example of the resulting power-law, galaxy starlight, dust torus and Fe II emission models fitted to the observed spectrum is illustrated in Fig. 1.

3.2.1 Reconstruction of the He I 10830 Å line

The near-IR metastable 2^3S helium line is reconstructed by isolating unabsorbed narrow and broad components and fitting these to the He I $\lambda 10830$ complex. The process is complicated by blending with the nearby $\text{Pa}\gamma$ line. It was noted that the epoch 6 near-IR spectrum showed no evidence of absorption features, therefore the narrow component was isolated and used as a template for all other epochs. The broad lines in the epoch 6 spectrum are relatively weak and symmetrical, therefore it was a simple process to isolate this narrow component by fitting the broad components of both the He I $\lambda 10830$ line and the $\text{Pa}\gamma$ line with two Gaussians each. At epochs 1–5, the broad emission components of He I and $\text{Pa}\gamma$ are not symmetrical. To deal with this, a broad emission template was extracted from the $\text{Pa}\beta$ complex at

Table 1. Quasi-simultaneous near-IR and optical observations.

Optical Observations					
Epoch	Date	Position angle °	Airmass	Exp. time (seconds)	Signal/Noise at 4000 Å
1	2002 Apr 11	70	1.04	3 × 30	19.1
2	2004 May 28	90	1.30	2 × 30	10.1
3	2006 May 29	90	1.03	2 × 30	10.1
4	2007 Feb 9	90	1.05	2 × 30	12.0
5	2010 Feb 18	90	1.05	3 × 60	26.9
6 [†]	2015 Mar 14	254	1.10	3 × 180	16.2
Near-IR Observations					
Epoch	Date	Position angle °	Airmass	Exp. time (seconds)	Signal/Noise at 11 000 Å
1	2002 Apr 23	130	1.10	1800	243
2	2004 May 23	90	1.13	6 × 120	28.0
3	2006 Jun 12	90	1.22	10 × 120	78.4
4	2007 Jan 24	90	1.45	8 × 120	29.0
5	2010 Feb 27	188	1.06	10 × 180	240
6	2015 Feb 5	223	1.08	8 × 120	28.3

[†] This observation was undertaken with the WHT, all other optical spectra were obtained from the Tillinghast telescope.

each of these epochs by first identifying blended narrow components in the simpler epoch 6 spectrum using appropriate Gaussian models (listed in Table 2) and then subtracting them out at other epochs after appropriate scaling. Identification of the narrow component of He I $\lambda 10830$ and the Pa β blends is illustrated in Fig. 2.

These templates, together with a narrow Gaussian representing the narrow component of Pa γ , were simultaneously scaled to the observed blend to produce a reconstruction of the unabsorbed He I $\lambda 10830$ complex. An example of the individual components used to fit the blend is illustrated in Fig 3.

3.2.2 Reconstruction of the He I 20587 Å line

The helium emission line at 20587 Å is very weak compared to the triplet state emission line in the near-IR spectrum, as is the corresponding blueshifted absorption. To reconstruct this emission line at each epoch, the narrow component of the He I $\lambda 10830$ line was interpolated onto the wavelength of the 20587 Å line and underwent scaling and linear flux shift (at most 1 wavelength bin) to match the red (unabsorbed) side of the emission line by means of chisquare minimisation. No broad component of this line was discernible, therefore no attempt was made to produce a broad component as part of the reconstruction. An exception to this method was that used for the epoch 5 reconstruction, where the absorption is sufficiently strong that the narrow emission line is lost in the absorption trough. In this case, the scale factor between the narrow component at 10830 Å and 20587 Å was assumed to be the same as that at epoch 6, since changing line ratios in response to ionizing continuum changes in the relatively extended narrow line region only happen over relatively long time periods. The final reconstructed line+continuum emission templates at each epoch are indicated in Fig. 4. It proved difficult to fit an accurate continuum template to this region of the spectrum, so

the continuum was assumed to be a flat flux level at the line base. The resultant lack of deconvolution between the various components (power-law, torus and host galaxy emission), together with the absorber's singlet structure, means only lower column density limits can be calculated using this line.

3.2.3 Optical spectral region < 4000 Å

The unabsorbed emission at the blue end of the optical spectra is a complex blend of several different contributing sources. It is necessary to model the unabsorbed emission in this region accurately due to the weakness of the He I $\lambda 3889$ feature. Hydrogen emission includes higher order Balmer series lines as well as the Balmer continuum discontinuity at 3646 Å which, given its observed wavelength shift and high degree of broadening, also contributes excess flux to this region. The narrow components of the Balmer series lines are straightforward to calculate, as it can be assumed that they form in a low-density environment where the dominant process generating the lines is Case B recombination.

The narrow line intensities can be calculated by referring to the theoretical H β ratios from Osterbrock & Ferland (2006) and assuming the widths are the same as for the narrow component of H β . The H α and H β emission profiles were modelled as three Gaussians (two for the broad component and one for the narrow component), an example fit is illustrated in Fig. 5. It was found that the narrow component H α /H β flux ratios were always greater than those predicted by theory. This was assumed to be due to intrinsic dust extinction of the form observed in the SMC bar with $R_V=2.74$ (Gordon et al. 2003). To correct for this reddening, test $E(B-V)$ values were incrementally varied and applied to the theoretical ratios until the observed H α /H β ratios were correctly predicted. The epoch 1 optical spectrum was excluded from the subsequent absorption line analysis due to the multi-peaked nature of the H α line, rendering an

Table 2. Narrow lines subtracted from Pa β blend.

Blended narrow line	Central wavelength (Å)
[S IX]	12 520
[Fe II]	12 567
[Fe II]	12 790
Pa β	12 818
Unknown, possibly Fe II or Ne I	12 888
[Fe II]	12 943
[Fe II]	13 205

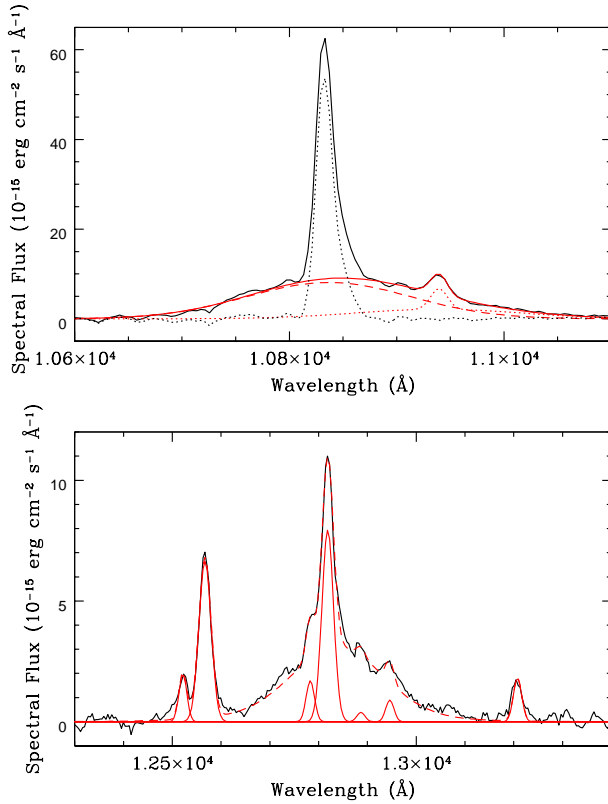


Figure 2. *Top panel:* Isolation of He I narrow component (black dotted line) from epoch 6 by subtraction of the He I broad component (red dashed line) and Pa γ broad+narrow line (red dotted line). The total subtracted model is represented by the red solid line, while the black solid line is the observed He I blend. *Bottom panel:* Epoch 6 observed Pa β blend (solid black line) and Gaussian-modelled narrow lines (solid red lines). The red dashed line indicates the total line-blend model. Modelled narrow lines were subtracted to leave a broad template at epochs 1–5. Both panels show spectra after subtraction of the underlying continuous emission.

accurate fit very difficult to attain. This was not expected to alter the conclusions of this investigation as no obvious absorption is present at this epoch in either spectrum.

The broad components of these lines do not form in a low-density environment, meaning that electron impact excitation must be taken into account when calculating their intensities. In Popović (2003), applying Boltzmann plots to

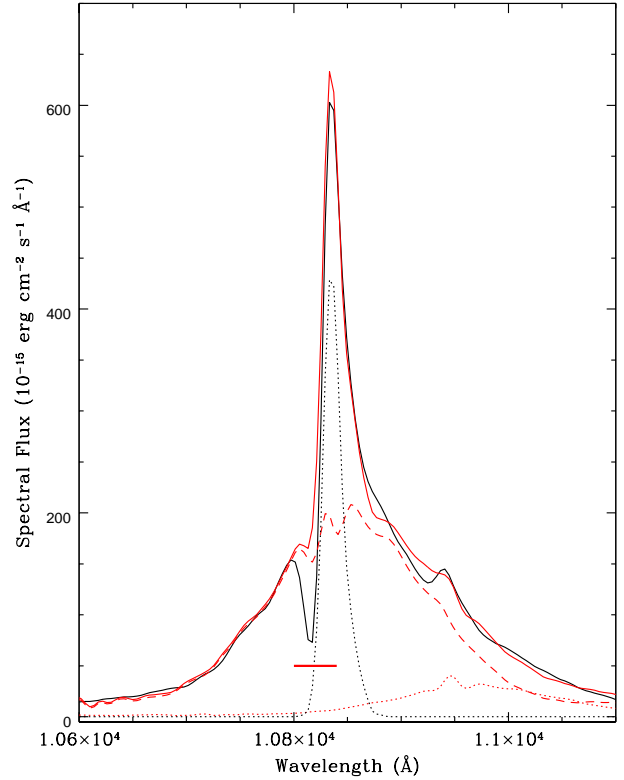


Figure 3. Fitted components to the He I $\lambda 10830$ complex at epoch 5 after subtraction of the continuous emission. The He I narrow component is represented by the black dotted line, the He I broad component by the red dashed line, and the Pa γ broad+narrow emission by the red dotted line. The total unabsorbed model is represented by the red solid line, while the black solid line is the observed He I blend. Both broad components were derived from the Pa β broad template. The horizontal red line indicates the wavelengths spanned by an absorption feature.

broad Balmer line intensities revealed that the broad emission line regions of several AGN, including NGC 4151, were in partial local thermodynamic equilibrium (PLTE). We make the assumption of PLTE in this case and use Equation 2 in Popović (2003) to calculate the broad component intensities based on the strengths of the lower order lines, assuming that the widths are the same as that of the broad H β component. The Balmer continuum can be modelled by

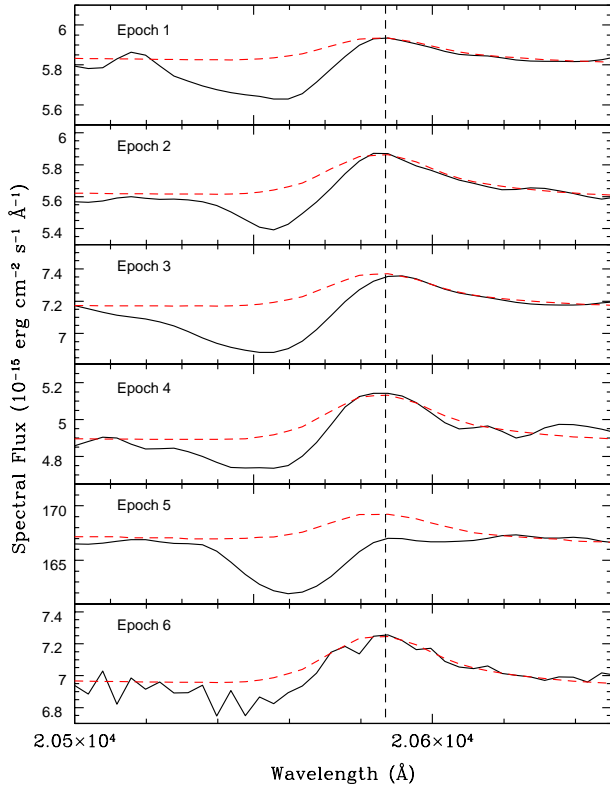


Figure 4. Observed spectrum (solid black line) and unabsorbed reconstruction (dashed red line) in the spectral region near He I $\lambda 20587$ (line centre indicated by the vertical black dashed line).

relating the Balmer continuum jump at 3646 \AA to the electron temperature in the line forming region, assuming the plasma is optically thin and has a single electron temperature (Grandi 1982; Wills et al. 1985). This results in the following equation

$$F_{\nu}^{\text{BC}} = F_{\nu}^{\text{BE}} e^{(-h-\nu_{\text{BE}})/(kT_e)}, \quad (1)$$

where F_{ν}^{BC} is the Balmer continuum flux at frequency ν , F_{ν}^{BE} is the flux at the Balmer edge, k is the Boltzmann constant, h is Planck’s constant and T_e is the electron temperature. The study of Jin et al. (2012) indicated that, in order to get an acceptable Balmer continuum fit to the spectrum of PG 1427+480, the position of the discontinuity needed to be shifted redward by 100 \AA and broadened by 6000 km s^{-1} . A visual inspection of the Balmer edge calculated at each epoch with no broadening or shifting indicated a similar process was required for our optical spectra. A possible explanation for this wavelength shift could be Stark broadening if the electron density in the Balmer continuum emission region is much higher than in the BLR (Pigarov et al. 1998), suggesting this region may lie in the illuminated accretion disc rather than the BLR clouds (Jin et al. 2012; Collin-Souffrin & Dumont 1990). The Balmer continuum was fitted to our spectra by simultaneously and iteratively shifting and broadening the Balmer jump until a good fit was achieved. A shift of $\sim 100 \text{ \AA}$ and a broadening of $\sim 24000 \text{ km s}^{-1}$ were found to give the best fit for the Balmer continuum.

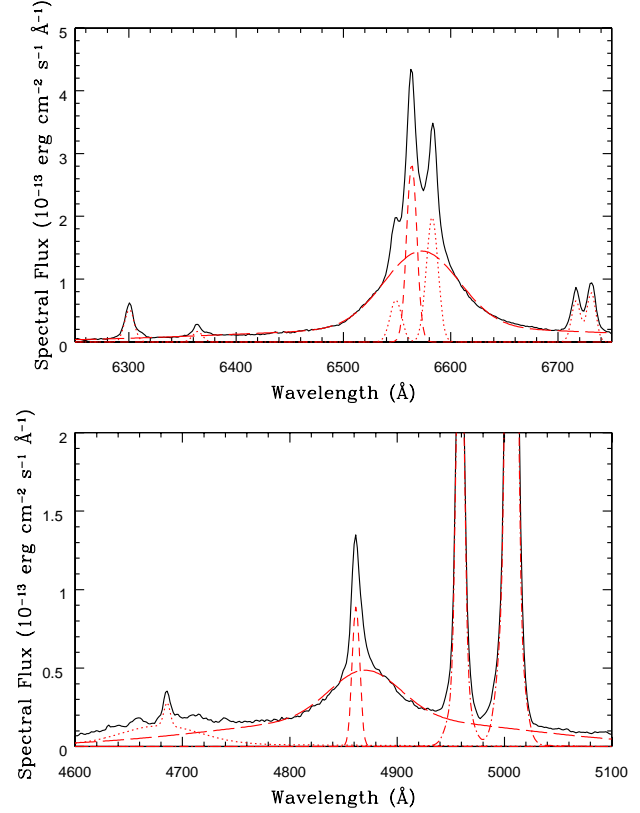


Figure 5. Gaussian fits to the spectral region of H α (top panel) and H β (bottom panel) at epoch 5. In both panels the solid black line represents the observed spectrum with the underlying continuous emission subtracted. The short-dashed and long-dashed red lines represent the Balmer line narrow and broad components respectively. The dotted red lines in the top panel represent the blended narrow emission lines, while in the bottom panel the dotted red line represents the blended He II emission feature. The dot-dashed red lines in the bottom panel represent the blended [O III] doublet components.

Once an accurate model of the hydrogen emission has been achieved, this must be added to the He I $\lambda 3889$ emission complex to create a complete “pseudocontinuum” from which the depth of the absorption feature can be measured. This feature is blended with the [Ne III] $\lambda 3868$ line, which therefore also needs to be reconstructed. Since, as already discussed, the epoch 6 near-IR spectrum shows no evidence of metastable He I absorption, the narrow component of the 10830 \AA line can be used as a template for the He I $\lambda 3889$ line. No broad component for this line is required as it is so weak as to be indiscernible. Given the large ratio between the oscillator strengths of the near-IR and optical lines and the lack of absorption in the near-IR line, it is unlikely that epoch 6 shows any metastable helium absorption corresponding to the optical transition. Therefore, the epoch 6 near-IR He I narrow emission line was scaled to match the red (unblended) side of the corresponding optical emission profile. The [Ne III]+He I blend could then be fitted at epoch 6 by adding to this He I template a [Ne III] template, generated by inverting the unblended blue side of the observed line to reconstruct the blended red side. These

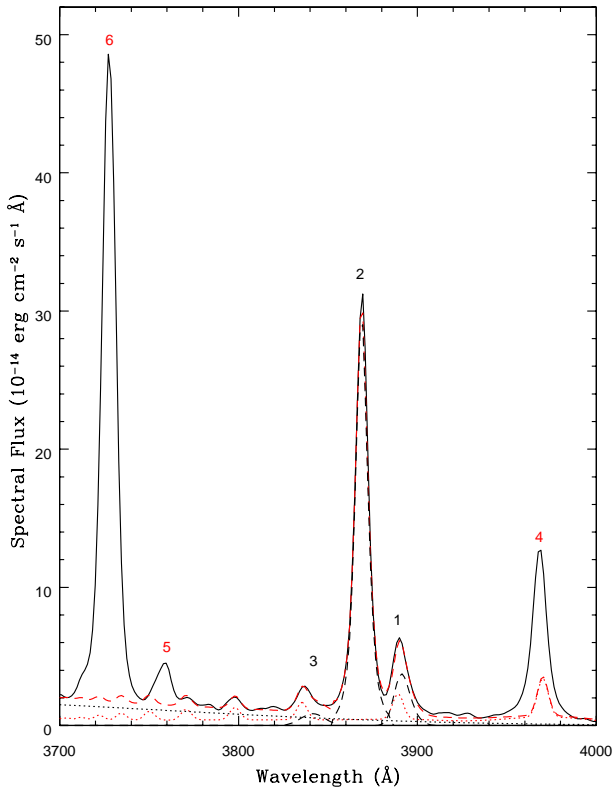


Figure 6. Spectral fitting in the <4000 Å region at epoch 6. The solid black line is the observed spectrum with the continuous emission components (power-law, galaxy starlight and broad Fe II) subtracted. The dotted black line is the broadened and shifted Balmer continuum emission model and the dotted red line is the Balmer BLR+NLR emission model. The dashed black lines underneath labels '1' and '2' are the reconstructed He I $\lambda 3889$ and [Ne III] $\lambda 3868$ emission lines respectively, while that labelled '3' is an unknown line modelled with a broad Gaussian component. The red dashed line is the total reconstructed spectrum made up of the sum of all aforementioned emission models. Labels '4', '5' and '6' indicate those lines sufficiently far from the helium line that reconstruction was not deemed necessary.

two templates were then added to the calculated Balmer emission components along with a broad (~ 3000 km s $^{-1}$) Gaussian to account for unknown emission at 3840 Å. This completes the total unabsorbed reconstruction at epoch 6, as shown in Fig. 6. Epochs 1–5 were fitted using the calculated Balmer emission together with appropriate scaling of the epoch 6 [Ne III] and He I templates. The total unabsorbed reconstruction of the epoch 5 spectrum (which contains an absorption feature) is shown in Fig. 7.

3.3 Singlet and triplet state metastable helium column densities

The simplest method of measuring outflow column densities is to assume that the absorber is unsaturated and covers 100 per cent of the emission region. This requires a simple integration across the absorber profile (Savage & Sembach 1991) given by

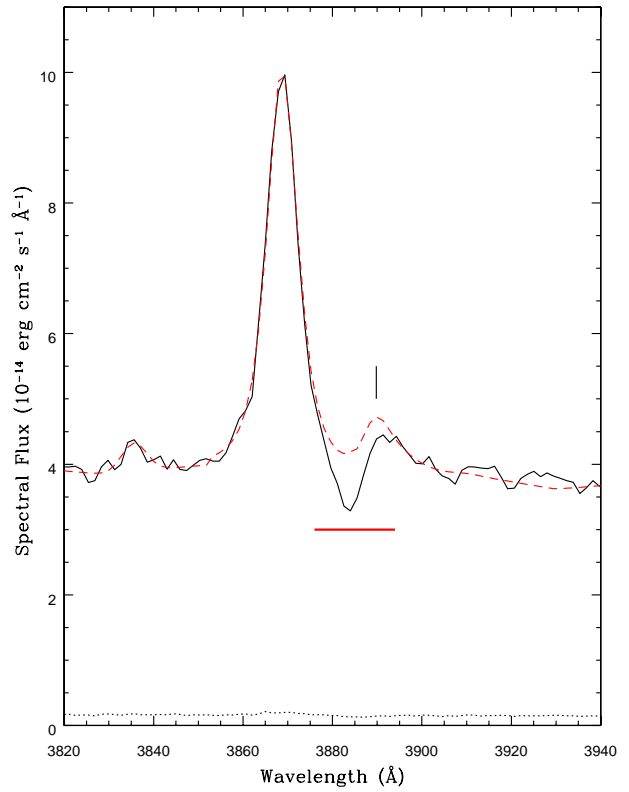


Figure 7. Epoch 5 total optical spectrum (solid black line) and its total reconstruction (red dashed line) near the He I $\lambda 3889$ line. The horizontal solid red line indicates the wavelength span of the absorber, while the vertical solid black line indicates the location of the He I emission line centroid. The dotted black line indicates the errors on the observed spectrum.

$$N_{ion} = \frac{m_e c}{\pi e^2 f \lambda} \int \tau(v) dv, \quad (2)$$

where N_{ion} is the ionic column density, v is the velocity relative to the laboratory rest-frame wavelength of the transition, m_e is the electron mass, c is the speed of light, e is the elementary charge, f is the oscillator strength, λ is the laboratory rest-frame wavelength and $\tau(v)$ is the optical depth at a given velocity. For this investigation wavelength measurements were converted to velocities relative to emission line centre. Sources of error include the point-to-point uncertainty in the flux values and a fractional error associated with the reconstructed spectrum. This fractional error was derived from the root-mean-square of the normalised difference values between the reconstructed and observed spectra at ~ 1300 km s $^{-1}$ either side of the spectral region spanned by velocity bins which show absorption in at least one epoch. Calculations were performed separately for the optical and near-IR spectra at epochs 2–6 and 1–6 respectively. The emission region is assumed to be that generating the modelled power-law continuum emission over the span of the absorption feature (see §3.3.1 for justification). The near-IR emission-region-normalised 2^3S profiles at epochs 1 to 5 are shown in Fig. 8 (epoch 6 has zero absorption by definition). Absorption is apparent at epochs 3–5, with the epoch 5 absorber occupying, on average, a region of lower

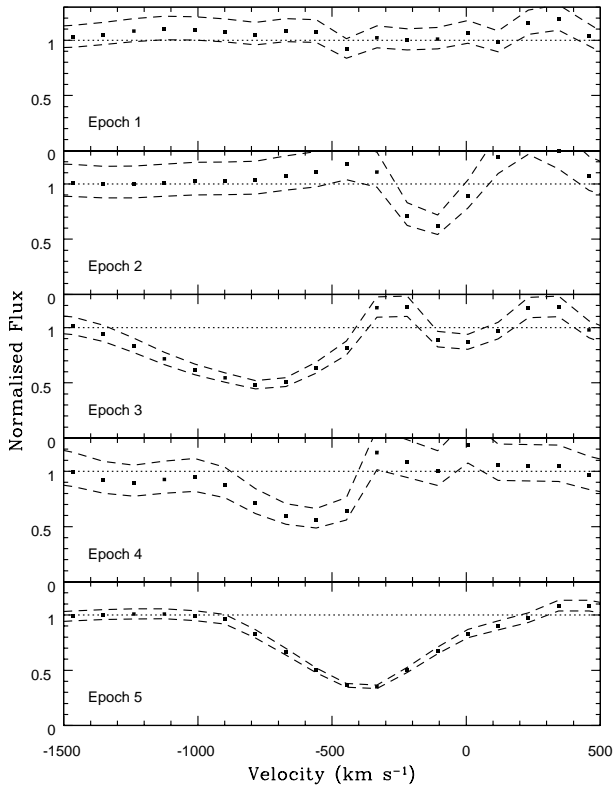


Figure 8. He I $\lambda 10830$ absorber profiles across epochs 1 to 5. Black squares indicate the residual flux at each velocity bin. Dashed lines show the envelope of values allowed by the fractional error in the emission profiles.

(less negative) outflow velocity compared to epochs 3 and 4. This suggests a possible separate physical origin of the epoch 5 absorber compared to earlier epochs, especially at $v > -400$ km s $^{-1}$.

Using the unabsorbed reconstructions in the spectral region of the He I $\lambda 20587$ line shown in Fig. 4, a value of the column density in this state can be estimated from the normalised spectral profile of the absorbed region (excluding the narrow emission line as the NLR is probably uncovered by the absorber). Since the He I transition at 20587 Å is a singlet, only a lower limit for the column density can be obtained using direct integration of the profile, which will be an underestimate if partial coverage and saturation are present. However, we would expect these limits to be close to the true value given the shallowness of the absorber (Leighly et al. 2011). As mentioned in §3.2.2, column densities also need to be lower limits due to a lack of separation of the various emission sources at the wavelengths spanned by the singlet state absorber. The normalised absorption profiles are shown in Fig. 9. The derived column densities for both 2^3S (from the 3889 Å line and the 10830 Å line) and 2^1S state helium are recorded in Table 3.

The unreliability of the optical measurements (due to the quality of the spectrum, the weakness of the continuum and the weakness of any 3889 Å He I absorber) is clear from these values for all but epoch 5, which is the only observation having a column density of greater than 2σ significance

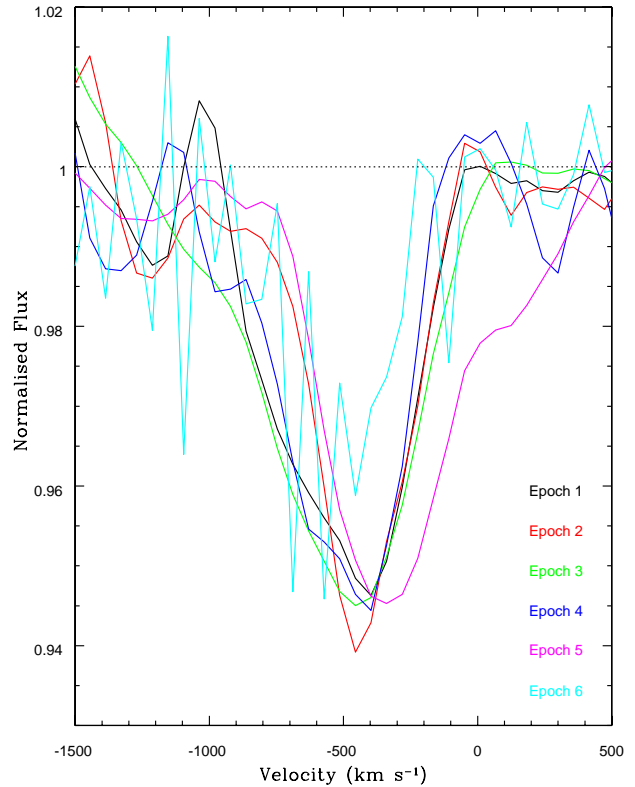


Figure 9. He I $\lambda 20587$ absorber profiles across epochs 1 to 6. Each profile is colour-coded by epoch as shown in the bottom right.

(4.8σ). The strength of the near-IR absorber allows more reliable measurements to be made of absorber variability, which will be discussed further in §5. The 2^1S column density values are mutually consistent across the epochs, so no variability in this absorber is identifiable. This absorber is weak and the position of underlying emission is uncertain, so the lack of variability is not considered indicative.

3.3.1 Partial covering analysis of epoch 5

The significance of the optical absorber at epoch 5 allows a partial coverage analysis to be performed at this epoch by using both the optical and near-IR absorbers. We use a method similar to that adopted by Leighly et al. (2011), applying a pure partial coverage model (PPC) to the optical and near-IR 2^3S He I absorption components. Although the investigation of that paper also included a power-law inhomogeneous model, this yielded column densities not significantly different from the PPC model in that study, and hence it is not used in this investigation. The PPC model was originally applied to quasar absorption lines (Hamann et al. 1997; Arav et al. 1999) and relates the observed flux density within an individual wavelength bin to the total flux from the emission source and the covering fraction as follows:

$$\frac{I_{\text{app}}}{I_0} = C e^{-\tau} + (1 - C), \quad (3)$$

Table 3. Apparent column densities calculated at each epoch over the optical and near-IR absorption regions. Epoch 1 is excluded from the optical analysis due to the lack of a reconstructed profile. Zero values include negative values within the error limits.

Epoch	Optical 2^3S column density (10^{13} cm^{-2})	Near-IR 2^3S column density (10^{13} cm^{-2})	2^1S column density (lower limit) (10^{13} cm^{-2})
1	N/A	0 ± 0.98	0.148 ± 0.035
2	77.7 ± 121	0.12 ± 1.47	0.134 ± 0.046
3	88.1 ± 120	2.73 ± 0.52	0.177 ± 0.028
4	79.9 ± 40.3	1.45 ± 0.59	0.146 ± 0.068
5	28.3 ± 5.87	3.44 ± 0.30	0.176 ± 0.021
6	0 ± 108	0 ± 1.17	0.111 ± 0.041

where I_{app} is the apparent flux, I_0 is the flux from the emission region, C is the fraction of the total emission covered by the absorber and τ is the optical depth. In order to compare the normalised depth of each component, the normalised near-IR absorption line spectrum was interpolated into the velocity space of the normalised optical spectrum with velocity bin width $\sim 113 \text{ km s}^{-1}$. By taking into account the 23.3 times greater optical depth of the near-IR component as compared to the optical component, the strengths can be compared using the equation

$$\left(\frac{I_{\text{op}} - 1}{C} + 1\right)^{23.3} - \frac{(I_{\text{IR}} - 1)}{C} - 1 = 0, \quad (4)$$

where I_{op} and I_{IR} are the normalised fluxes of the optical and near-IR components respectively.

Before performing the calculations it is necessary to identify the emission region which is covered by the absorber along the line-of-sight (providing I_0). An outflow associated with the active nucleus will not absorb a significant portion of the galaxy flux. The optical absorber is deeper than the combined BLR and torus (blackbody) emission, so sole coverage of one or both of these regions is ruled out. This leaves three possibilities for the absorbed region: power-law continuum only, continuum+BLR and continuum+BLR+torus. Identification of the best option is achieved using the condition $I_{\text{op}} \geq I_{\text{IR}} \geq I_{\text{op}}^{23.3}$, which is necessary for the validity of Equation 4. Assuming continuum coverage only, all nine velocity bins showing significant absorption in the stronger (near-IR) component are valid, while the other possibilities (continuum+BLR and continuum+BLR+torus) result in three and five bins violating the condition respectively. The emission region is therefore assumed to be that producing the power-law continuum, which is used as I_0 in all calculations in this paper involving 2^3S helium.

The calculation of column density relies on finding a solution for C in Equation 4. Unlike the case of a UV absorber such as Si IV (with doublet optical depth ratio 2:1), Equation 4 has no analytic solution. Therefore, a numerical test is performed by varying C in steps of 0.001 between 0 and 1 at each velocity bin. At each step, the error associated with the expression on the left-hand-side of Equation 4 is calculated. Solutions of C within error limits therefore correspond to those steps where the magnitude of the expression minus its error is less than zero, as illustrated in Fig. 10. This test is carried out at all nine velocity bins which satisfy $I_{\text{op}} \geq I_{\text{IR}} \geq I_{\text{op}}^{23.3}$, with the normalised absorption profiles shown in Fig. 11. It is clear, given the large theoretical component ratio, that the near-IR absorber must

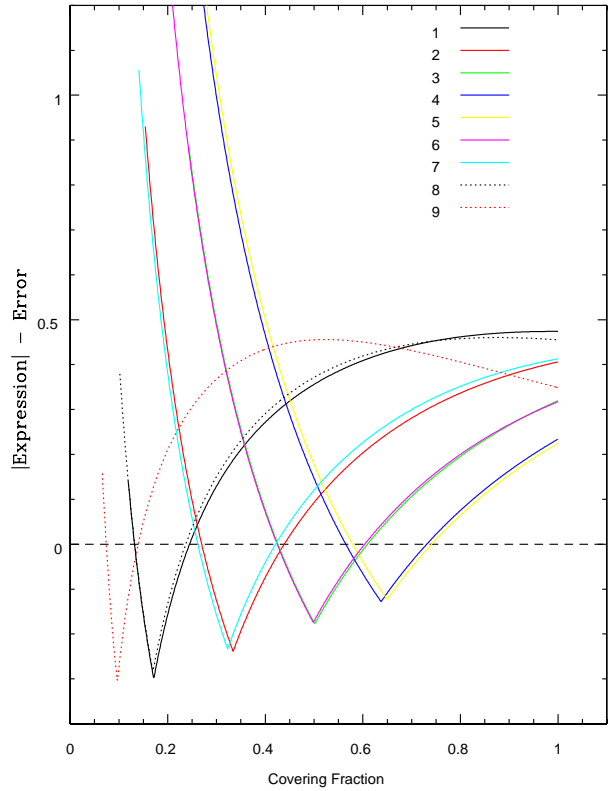


Figure 10. Curves representing the magnitude of the left-hand-side of Equation 4, minus the associated error, for covering fractions between 0 and 1 at each valid velocity bin (line number labels in top right correspond to those in Fig. 11). Where each curve crosses zero (two points) are taken as the lower and upper limits of C at that bin.

be saturated across the region spanned by the nine velocity bins. In such a case the absorber profile is determined by the covering fraction. The column density can be calculated in a similar way to Equation 2 as follows

$$N_{\text{ion}} = \frac{m_e c}{\pi e^2 f \lambda} \int \tau(v) C(v) dv, \quad (5)$$

giving a triplet state metastable helium column density of $3.47^{+0.99}_{-1.05} \times 10^{14} \text{ cm}^{-2}$. This is therefore a well constrained absorber suitable for further analysis (see §4.)

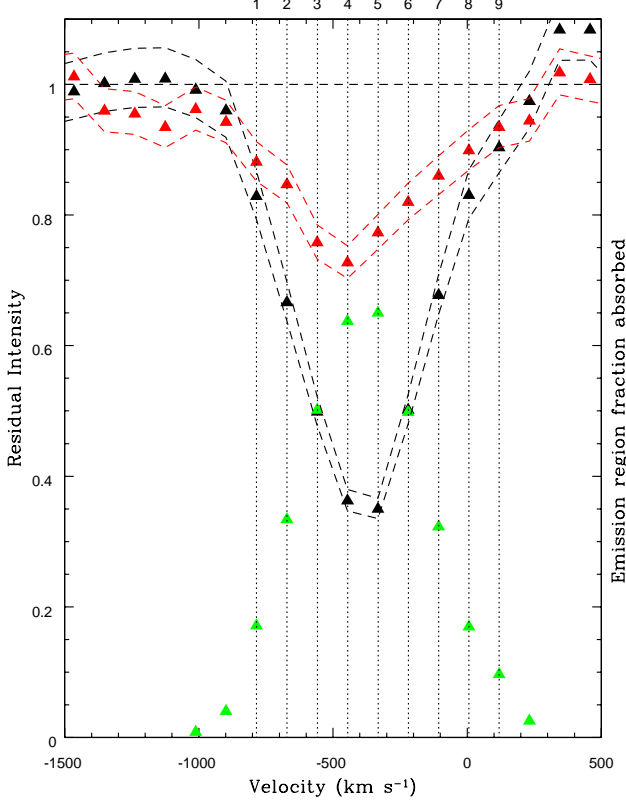


Figure 11. Normalised absorption profiles of triplet state metastable helium absorption at 3889 Å (red triangles) and 10830 Å (black triangles), representing the residual intensity at each velocity bin. Velocity bins which satisfy $I_{\text{op}} \geq I_{\text{IR}} \geq I_{\text{op}}^{23.3}$ are located at velocities marked by dotted vertical lines and are assigned numerical labels in order of increasing (positive direction) velocity, with negative velocities indicating outflow from the emission source. Green triangles represent the continuum emission absorbed at each velocity bin as derived from the near-IR spectrum. Dashed lines show the envelope of values allowed by the fractional error in the emission model.

4 PHOTOIONIZATION SIMULATIONS

4.1 CLOUDY simulations

In order to locate the epoch 5 triplet state absorber in ionization parameter, number density and column density space, grids of photoionization simulations were calculated. The photoionization simulations calculated for this paper were performed using CLOUDY version c13.02 (Ferland et al. 2013), for which the setup was similar to that described in paragraph 1 of §3.1 in Leighly et al. (2011). Simulations were available which utilised a triplet state He I column density of $n_{\text{He}}(2^3S) = 3.67 \times 10^{14} \text{ cm}^{-2}$, well within the errors on the epoch 5 absorber determined from the PPC analysis. These simulations are those discussed in this section.

The ionization parameter (U) is a useful quantity for measuring the ratio of Lyman continuum photons to hydrogen atoms as follows

$$U = \frac{Q(H)}{4\pi r^2 n_{\text{H}} c}, \quad (6)$$

where $Q(H)$ is the number of Lyman continuum photons

produced by the ionizing source per second, r is the radial distance from the photon source and n_{H} is the hydrogen number density. We use an input spectral energy distribution (SED) that follows the shape of the AGN continuum described in Korista et al. (1997) and we adopt solar abundances from Grevesse & Sauval (1998), Holweber (2001), and Allende Prieto et al. (2001, 2002). This continuum is assigned to the CLOUDY calculations by using the “AGN Kirk” command.

Balmer absorption was detected in NGC 4151 by Hutchings et al. (2002), arising from the $\text{H}\beta$ transition. In Leighly et al. (2011), the lack of Balmer absorption in the quasar FBQS J1151+3822 was used to set an upper limit on the $n=2$ hydrogen state column density. The spectral region of $\text{H}\beta$ at epoch 5 was examined to determine whether or not $\text{H}\beta$ absorption was present. This employed the multiple Gaussian reconstruction used previously (see Fig. 5) as the unabsorbed reconstruction. No absorber is apparent from a visual inspection of the spectrum and the reconstruction. This lack of absorption can be used to set limits on the allowed ionization parameter and total hydrogen column density of the absorber as described in §4.3.

Our calculations require two runs of the code over each grid. The first run is used to find the thickness of the absorbing cloud to be integrated through to reach the spectroscopically-determined column density of helium in the 2^3S metastable state at epoch 5. This allows the total hydrogen (N_{H}) and 2^1S state helium column densities to be calculated. The second run integrates through to the N_{H} values determined from the first run to find the hydrogen level populations, which can then be used to determine if a particular gridpoint exceeds the allowed Balmer absorption. Spectroscopic constraints on the column density of helium in the 2^1S state are lower limits, meaning that CLOUDY-derived values must exceed the observed value ($1.76 \times 10^{12} \text{ cm}^{-2}$ from Table 3) to be considered valid.

The CLOUDY output provides the fraction of helium in the sum of all singlet states at each principal quantum state rather than the individual singlet states at different total azimuthal quantum numbers. Helium in the $n=2$ singlet state exists in both $1S$ and $1P$ configurations, meaning the latter of these must be taken into account to derive the fraction in the 2^1S state. This state is formed by the combined effect of $\text{He}^+ + e^-$ recombinations and collisional excitation from the 2^3S metastable state. Approximately one third of helium recombinations to a singlet state of $n=2$ or higher ultimately results in population of the 2^1S state, while the rest lead to the ground state. Therefore, using the recombination and collisional rate coefficients derived from Smits (1996); Benjamin et al. (1999) and Bray et al. (2000) respectively as listed in Osterbrock & Ferland (2006), the fraction of helium in the 2^1S state at each CLOUDY output zone can be found as follows

$$F(2^1S) = F_s \times \frac{\alpha_{c1} n_{\text{He}}(2^3S) + 0.33 \alpha_{\text{rec}} n_{\text{He}+}}{\alpha_{c1} n_{\text{He}}(2^3S) + \alpha_{c2} n_{\text{He}}(2^3S) + \alpha_{\text{rec}} n_{\text{He}+}}, \quad (7)$$

where, for a specific zone, $F(2^1S)$ is the fraction of helium in the 2^1S state, F_s is the CLOUDY-calculated value of the helium fraction in the $n=2$ singlet states, α_{c1} is the 2^3S-2^1S collisional rate coefficient, α_{c2} is the 2^3S-2^1P collisional rate coefficient, $n_{\text{He}}(2^3S)$ is the number density of helium in the 2^3S state, $n_{\text{He}}(2^1S)$ is the number density of helium in the

2^1S state and α_{rec} is the sum of the recombination rate coefficients to all singlet states at $n=2$ or above. The bulk of the zone temperatures are within the ranges listed in tables 2.4 and 2.5 of Osterbrock & Ferland (2006), therefore linear interpolation is used to find the appropriate rate coefficients at individual zones. For those zone temperatures outside the ranges listed, linear extrapolation is used.

4.2 First coarse run

It was convenient to initially generate a “coarse” grid measuring 8×7 using a range in ionization parameter U of $-2.5 \leq \log U \leq 1.0$ in steps of 0.5 dex and a range in hydrogen number density n_H of $3.0 \leq \log(n_H/\text{cm}^{-3}) \leq 9.0$ in steps of 1.0 dex. Having found the gridpoints which satisfy the conditions derived from the spectra, a “fine” grid could then be calculated to narrow down the allowed values in the parameter space neighbouring the allowed coarse gridpoints. The gas hydrogen column density at each gridpoint was set equal to $\log N_H = 24.5 + \log U$ to allow the code to integrate through the relatively high-ionization region occupied by 2^3S He I. The grid was generated by performing the following steps: (i) The He I 2^3S -state column density output from CLOUDY is compared to the epoch 5 spectroscopically-derived value. Gridpoints which produce values lower than this are ruled out, (ii) for those gridpoints that satisfy condition (i), the 2^3S He I number density in each output zone generated by the code is calculated by multiplying the fraction of helium in this state by the helium abundance and n_H , (iii) the 2^1S He I number density in each output zone is found by calculating $F(2^1S)$ in each zone using Equation 7 and multiplying the result by the helium abundance and n_H , (iv) the absorber thickness is found by performing the integral $\int n_{He}(2^3S) dr$ through each zone from the irradiated face of the cloud inward until the epoch 5 column is reached, with the radius at which this value is reached giving the total thickness, (v) this integration is performed over the same zones as in (iv) to find the 2^1S column density using $\int n_{He}(2^1S) dr$, and (vi) the total thickness is multiplied by n_H for the gridpoint in question to find the hydrogen column density N_H .

4.3 Second coarse run

The absence of $H\beta$ absorption can be used to obtain an upper limit on the column density of hydrogen in the $n=2$ state and therefore rule out gridpoints where the CLOUDY models suggest this upper limit is exceeded. To do this, CLOUDY is run for a second time over the coarse grid, using a method very similar to that described in paragraph 3 of §3.1 in Leighly et al. (2011). The normalised epoch 5 profile shape for the He I $\lambda 3889$ absorber is assumed to be the shape that any hydrogen absorption would follow. Balmer absorption can arise from hydrogen atoms in either of the two $n=2$ states (2^2S or 2^2P), so to calculate the correct column density the relative populations of atoms in each state must be known. Using the N_H values obtained from the first run, CLOUDY was set to integrate through to these values and then run for a second time to determine the hydrogen $n=2$ population values.

The minimum H I $n=2$ column density at which a measurement would become significant is estimated by replacing

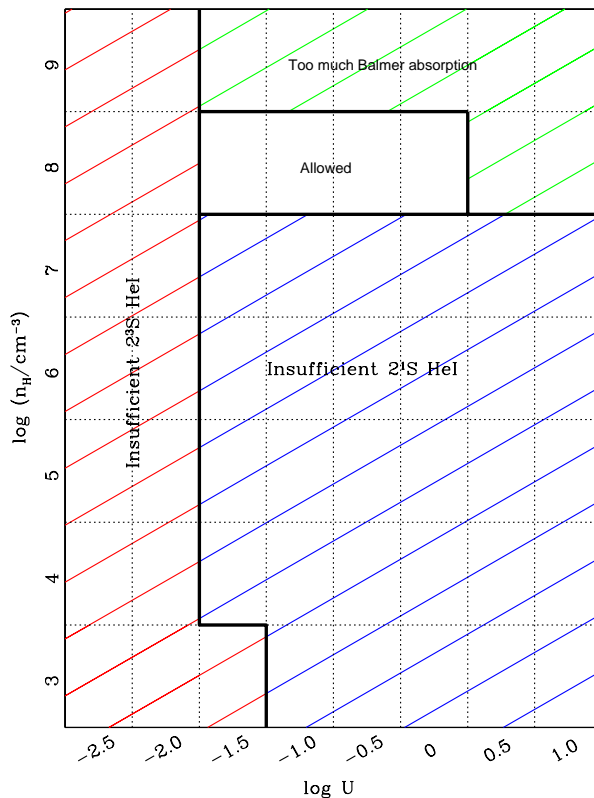


Figure 12. Allowed and ruled out coarse gridpoints (gridpoints are represented by rectangles enclosed by dotted lines). Gridpoints showing insufficient metastable 2^3S helium absorption were ruled out first (red shaded area). Gridpoints showing too much Balmer absorption were ruled out second (green shaded area). Gridpoints showing insufficient helium in the 2^1S state were ruled out third (blue shaded area). The remaining allowed region is unshaded.

the $f\lambda$ value in Equation 5 by a weighted mean value which depends upon the proportion of atoms in each of the two hydrogen $n=2$ states and using the same $C(v)$ profile as was calculated for 2^3S He I. The depth at every velocity bin of this profile is then scaled by factors of between 0.001 and 1 in steps of 0.001, with the column density calculated at each step using Equation 5. The first value of the column density at which the 1σ uncertainty in the calculation is exceeded is assumed to be the maximum column density of hydrogen in the $n=2$ state. The constraints on the allowed coarse gridpoints obtained from the metastable Helium, $n=2$ singlet-state helium and maximum Balmer absorption are illustrated in Fig. 12

4.4 Fine grid simulation

A second set of CLOUDY simulations using the same two-run method described in §4.2 and §4.3 was undertaken to further constrain the absorber properties at a finer resolution. A new grid measuring 24×19 spanning the ranges $-1.9 \leq \log U \leq 0.4$ and $7.1 \leq \log(n_H/\text{cm}^{-3}) \leq 8.9$, both in step sizes of 0.1 dex, was generated. Given the minimum value of $N_{\text{limHe}}(2^1S) = 1.76 \times 10^{12} \text{ cm}^{-2}$ listed in Table 3, all $\log n_H$

values in the fine grid are allowed. No attempt is made to rule out gridpoints in $\log U$ space where the minimum singlet helium column density is not reached as the 2^1S He I column density is a weak function of $\log U$ at a given $\log n_H$ in the grid. Further use is made of the fine grid in the Discussion section (§5).

The presence of turbulence or differential velocity in the outflowing gas can reduce the Ly α optical depth and therefore lead to a higher gas density limit than that derived in these CLOUDY models. This is due to reduced pumping into the H I $n=2$ state. Given the FWHM of the absorber (~ 600 km s $^{-1}$) and the spectral resolution (~ 400 km s $^{-1}$) the turbulence or differential velocity of the line cannot be larger than ~ 500 km s $^{-1}$. However it is likely to be lower than this, given the saturated nature of the near-IR line (Arav 2004). Figure 22 (right panel) in Appendix C of Leighly et al. (2011) shows that, for a 2^3S He I column density of the same order-of-magnitude, the upper limit on $\log(n_H/\text{cm}^{-3})$ increases by about 1.5 dex at a turbulent velocity $v_{\text{turb}}=500$ km s $^{-1}$. At $v_{\text{turb}}<500$ km s $^{-1}$, the upper limit on $\log n_H$ rapidly declines with decreasing v_{turb} .

5 DISCUSSION

5.1 Variability mechanism

In §4, the calculations were performed exclusively for epoch 5 due to the relatively narrow constraints obtained on the column density for that absorber, made possible by the detection of metastable helium absorption in both the optical (3889 Å) and near-IR (10 830 Å) wavebands. All other epochs only detected a near-IR absorber, resulting in the calculation of lower column density limits only. Although absorption variability cannot be detected in the optical waveband, there is significant variability in the near-IR profile as indicated in Table 3. There are two main possibilities for this variability mechanism, either (a) changes in the ionization state of the gas under the influence of a varying incident ionizing continuum, or (b) the fraction of the emission source covered by the absorber changes over time due to the absorber’s motion across the line-of-sight. These possibilities are now examined in detail. We only consider velocity space occupied by the epoch 5 absorber due to the availability of the simulation results and the lack of constraints on the (possibly physically separate) absorber at higher outflow (more negative) velocities.

5.2 Are ionizing continuum changes responsible?

Many AGN are known to have variable continuum emission in the optical and UV wavebands. This is true of NGC 4151 which shows variability across X-ray, UV and optical wavebands on timescales ranging from hours/days to multiple years e.g. Edelson et al. (1996); Crenshaw et al. (1996); Kong et al. (2006). Ionization of gas in the AGN vicinity is mainly controlled by the incident extreme ultraviolet (EUV) flux originating from the continuum emission region. If the gas is sufficiently dense, resulting in short recombination timescales, changes in the strength of associated emission/absorption lines should be correlated with changes in the unobserved EUV continuum. It can be assumed that

Table 4. Epoch 6-normalised power-law continuum model fluxes at 4000 Å.

Epoch	Normalised flux
1	5.1 ± 0.8
2	2.5 ± 1.8
3	1.7 ± 1.3
4	1.0 ± 0.6
5	9.9 ± 0.8
6	1.0 ± 0.5

[†] value is unity by definition

the optical-UV power-law continuum extends into the EUV, meaning measurements of the behaviour of the optical continuum can be used as a proxy for (ionizing) EUV variations (Kriss et al. 1999). This is the basis of reverberation mapping, where it is known that changes in the broad emission lines correlate with changes in the optical continuum, e.g. Peterson et al. (1998). However, this correlation may not be true for all AGN absorption lines. Studies showing evidence for ionizing continuum driven variability in AGN absorption lines include Wildy et al. (2015); Wang et al. (2015).

To test the plausibility of ionization-driven variability, we measured the relative changes in the flux of the power-law continuum model. The photometric accuracy of the spectra is not sufficient to directly compare continuum strengths across the observational epochs. Instead we scale the flux using the forbidden narrow line [Ne III] $\lambda 3868$, which is not expected to vary between epochs due to the spatially extended nature of the NLR and the low responsivity of forbidden lines to ionizing flux changes. The following procedure is therefore undertaken. At each epoch we multiply the power-law model by the flux of the [Ne III] $\lambda 3868$ template before dividing by the flux of the epoch 6 template and finally dividing the result by the power-law model at epoch 6 (template construction was described in §3.2.3). As noted, no template was generated for epoch 1, so instead at this epoch we use the same flux ratio but over only the unblended (blue side) of the line after subtracting a local linear continuum. The results are flux-corrected continuum models normalised to epoch 6. The values recorded at 4000 Å for each epoch are displayed in Table 4. The continuum peak-trough periodicity is consistent with V-band photometry of NGC 4151 recorded in Guo et al. (2014), which overlaps our epochs 3–5.

If continuum changes are driving the variability, it is important to understand in what sense the absorber should respond. For the epoch 5 absorber, Fig. 13 shows a representative curve of absorber column density varying as a function of $\log U$ taken at example physical conditions allowed by the CLOUDY fine-grid simulation ($\log(n_H/\text{cm}^{-3})=8.2$, $\log(N_H/\text{cm}^{-2})=21.5$). Since $\log n_H$ is held constant, variations in $\log U$ must correspond to changes in ionizing photon flux. From epoch 1, the continuum drops from a high state to a low trough at epochs 3 and 4, before reaching to its highest value of all 6 observations at epoch 5. It then returns to a lower state at epoch 6. Given the shape of the column density response in Fig. 13, this pattern of continuum variability would have to explain the absence of the epoch 5 absorber at epochs 1 and 2 (possibly also absent at epochs 3 and 4)

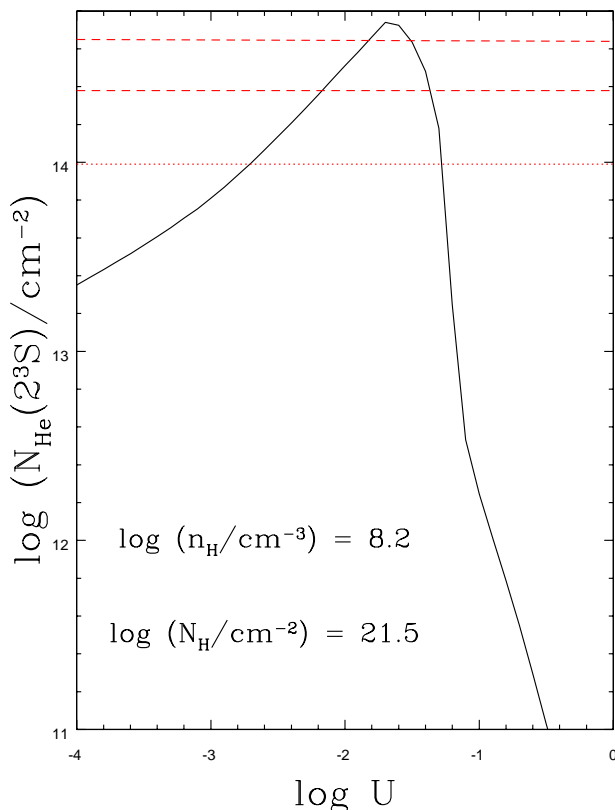


Figure 13. Behaviour of the 2^3S helium column density as a function of ionization parameter at a fixed hydrogen parameters of $\log(n_{\text{H}}/\text{cm}^{-3})=8.2$, $\log(N_{\text{H}}/\text{cm}^{-2})=21.5$. The epoch 5 (PPC model) absorber 1σ upper and lower column density limits are indicated by the dashed red lines. The dotted red line indicates the corresponding upper limit allowed by scaling the epoch 5 near-IR profile to the epoch 1 detection limit.

and its subsequent disappearance at epoch 6. This is consistent with a situation where $\log U$ is initially sufficiently low that any 2^3S He I absorption is undetectable (left of the peak in Fig. 13). The subsequent highly significant increase in continuum flux at epoch 5 boosts the metastable hydrogen column density to within the limits allowed by the partial coverage model, with the situation reversing between epochs 5 and 6.

From the example in Fig. 13, a reduction in $\log U$ of at least ~ 0.6 dex is required to remove the epoch 5 absorber from detectability at epochs 1 and 6. Given the fact that variability at ionizing wavebands can be many times greater than that in the optical e.g. Edelson et al. (1996), this is achievable, as the 4000 Å flux ratios at these epochs relative to epoch 5 are ~ 0.5 and ~ 0.1 respectively. The observations therefore support a situation where changes in the ionizing continuum incident on the absorber generate its measured variability.

5.3 A crossing-clouds model

The plausibility of changes in gas covering fraction as an explanation for the observed variability can be tested using a method similar to the “crossing disc” model applied in

Table 5. Fraction of emission region covered by absorber at each epoch

Epoch	Covering Fraction (A)
1	0 ± 0.09
2	0 ± 0.14
3	0.16 ± 0.06
4	0.10 ± 0.14
5	0.38 ± 0.03
6	0 ± 0.13

Capellupo et al. (2013, 2014). In this model a disc-shaped absorber moves across a disc-shaped emission source, changing the fraction of the emission covered and hence the apparent strength of the absorber. Given the values for the near-IR absorber recorded in Table 3, a plausible scenario that occurred in NGC 4151 over the course of the observations is that of a cloud starting to eclipse the AGN emission region as viewed from Earth at some point between epochs 2 and 3, reaching a peak coverage near epoch 5 before moving out of the line-of-sight prior to the epoch 6 observation. For the purposes of this study the model relates the velocity of gas across the line-of-sight to the crossing time as follows

$$v_c = \frac{\sqrt{\Delta A} D_c}{\Delta t}, \quad (8)$$

where v_c is the velocity of a disc-shaped cloud at right angles to the line-of-sight, ΔA is the change in the covering fraction of the emission source, D_c is the diameter of the region emitting the power-law continuum and Δt is the cloud crossing time available in the AGN rest-frame during the epoch interval. Assuming an optically thick, geometrically thin accretion disc (Shakura & Sunyaev 1973), an annulus at a given radial distance from the SMBH emits as a blackbody, with temperature dependent on distance. Therefore an estimate can be made of the size of the continuum region at the absorber centroid by considering all emission to be within a radius defined by the temperature giving the peak flux at this wavelength. This provides a value of $D_c = 1.1 \times 10^{16}$ cm. Covering fractions are calculated using the average normalised flux of the near-IR absorption component in the spectral range spanned by the epoch 5 absorber. These are listed in Table 5.

Covering fraction changes (ΔA) are computed across time intervals beginning or ending with epoch 5. Epoch 1 is excluded as the sense of any change between epochs 1 and 2 is completely unknown. Therefore, calculations for the intervals between epochs 2–5, 3–5, 4–5 and 5–6 are performed. Checking the consistency of the crossing-clouds model requires calculating the value of $\sqrt{\Delta A}/\Delta t$ and its associated error at each epoch interval used. These are listed in Table 6.

The velocity values calculated at the two epoch intervals showing significant absorption at both endpoints (3–5 and 4–5) are 420 km s^{-1} and 570 km s^{-1} respectively. The best value is therefore taken as the mean of these ($v_c = 495 \text{ km s}^{-1}$) under the assumption that crossing-clouds model is correct. One possible explanation for movement of absorbing gas across the line-of-sight to an AGN is that the gas is in orbit around the black hole with a lateral Keplerian velocity. The radial distance in such a scenario is $r_{\text{kep}} = GM/v_c^2$. Using the estimated mass of the black hole in

Table 6. Epoch interval-time-normalised $\sqrt{\Delta A}/\Delta t$ values

Epoch interval	$\sqrt{\Delta A}/\Delta t$ (10^{-9} sec^{-1})
2–5	3.38 ± 0.67
3–5	3.94 ± 0.66
4–5	5.37 ± 1.40
5–6	4.28 ± 0.63

NGC 4151 of $M_{\text{BH}} = 4.57 \times 10^7 M_{\odot}$ from Bentz et al. (2006), a value of $r_{\text{kep}} = 2.5 \times 10^{18} \text{ cm}$ (0.81 pc) is obtained.

If a crossing-clouds model were correct, consistency would be expected between values of $\sqrt{\Delta A}/\Delta t$ recorded at intervals 3–5 and 4–5. Additionally, intervals 2–5 and 5–6 should each show values consistent with or less than those at intervals 3–5 and 4–5, since the time the absorber spends outside the line-of-sight between epochs 2 and 3 and epochs 5 and 6 is unknown. From Table 6 it is clear that these conditions are met. Although this leads to self-consistency within the crossing clouds scenario, it does not provide conclusive evidence of its reality. Such evidence would require: (a) tightly constrained non-zero covering fractions across several epochs, and (b) knowledge that the same absorber is likely recorded at each epoch. It also seems coincidental within this model that the peak covering fraction should occur at maximum continuum strength. Therefore ionization change driven by the continuum is favoured as the variability mechanism.

5.4 Allowed parameter space and mass outflow rates of the absorber

The un-normalised SED used in the CLOUDY calculations can be appropriately scaled using the value of the bolometric luminosity given by $L_{\text{bol}} = 7.3 \times 10^{43} \text{ erg s}^{-1}$ (Kaspi et al. 2005). Using this scaled SED, we can estimate the distance from the ionizing continuum source to the incident surface of the epoch 5 absorber at each of the fine gridpoints described in §4.4, as shown in Fig. 14. Radial distances are within 0.49 pc of the continuum source for 90 per cent of all valid gridpoints, with an inner limit of 0.03 pc.

At a given $\log U$ gridpoint, total hydrogen column densities are a very weak function of $\log n_{\text{H}}$. Therefore only one set of points corresponding to $\log(n_{\text{H}}/\text{cm}^{-3}) = 7.9$, representing $\log N_{\text{H}}$ as a function of $\log U$, is indicated in Fig. 15. Allowed limits are $21.2 \leq \log(N_{\text{H}}/\text{cm}^{-2}) \leq 23.3$. Hydrogen column densities are required to calculate mass outflow rates, can be estimated from total hydrogen column densities using the method of Crenshaw et al. (2009) as follows

$$\dot{M}_{\text{out}} = 8\pi R N_{\text{H}} \mu m_{\text{p}} C_{\text{AGN}} |v_m|, \quad (9)$$

where μ is the mean atomic mass per proton ($\mu \sim 1.4$), m_{p} is the proton mass, C_{AGN} is the covering fraction of the outflow as seen from the active nucleus and v_m is the mean velocity of the outflow. Using an 80° opening angle (Hutchings et al. 1998), the covering fraction can be estimated as $C_{\text{AGN}} = 0.23$. The velocity of the (predominantly hydrogen) outflow is assumed to be approximately the same as the velocity centroid of the helium absorption ($v_m \sim 400 \text{ km s}^{-1}$). Examination of the outflow's hydrogen column density, radial distance

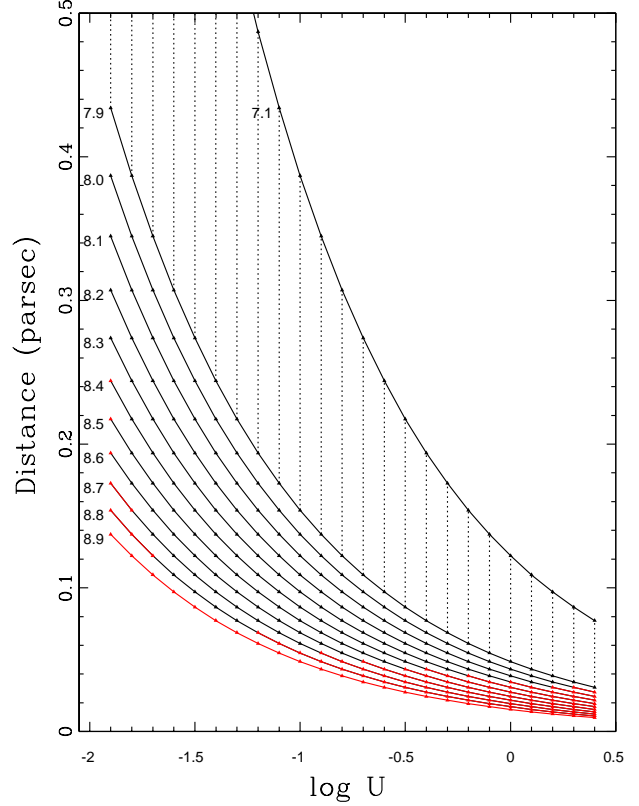


Figure 14. Radial location of the absorber as a function $\log U$ at $\log n_{\text{H}}$ values (indicated by numbers left of the respective curves). Fine gridpoints are indicated by triangles. Regions on the curve allowed by the Balmer absorption criterion are in black, regions predicting too much Balmer absorption are in red. All $\log U$ values in the fine grid are allowed at $7.1 \leq \log n_{\text{H}} \leq 7.9$ (region indicated by vertical dotted lines). Maximum distance (off-scale at $\log U = -1.9$, $\log n_{\text{H}} = 7.1$) is 1.1 pc.

and outflow rate across the permitted gridpoints allows constraints to be placed on these quantities. For the mass outflow rate the limits are $0.008 \leq \dot{M}_{\text{out}} (M_{\odot} \text{ yr}^{-1}) \leq 0.38$, which corresponds to a kinetic luminosity range of 4.11×10^{38} to $1.90 \times 10^{40} \text{ erg s}^{-1}$. The weakness of this outflow, with a kinetic luminosity of at most 0.026 per cent of the bolometric luminosity, indicates that it is not a significant contributor to galaxy feedback (Hopkins & Elvis 2010). The derived range in outflow rate overlies the relatively low mass accretion rate in NGC 4151 of $\dot{M}_{\text{acc}} = 0.013 M_{\odot} \text{ yr}^{-1}$ as calculated by Crenshaw & Kraemer (2007). At its lowest possible value, the outflow is about ~ 62 per cent of the accretion rate, however at its maximum it is ~ 29 times larger.

5.5 Comparison with previous observations

Since cases of absorption from metastable triplet state He I are effectively high ionization transitions, the observed absorption may also be visible in high ionization UV transitions resulting from species such as C IV and P V. Although no simultaneous UV spectra are available, the centroid of the epoch 5 absorber is similar to the 'D+E' feature described in Kraemer et al. (2005, 2006) and Crenshaw & Kraemer

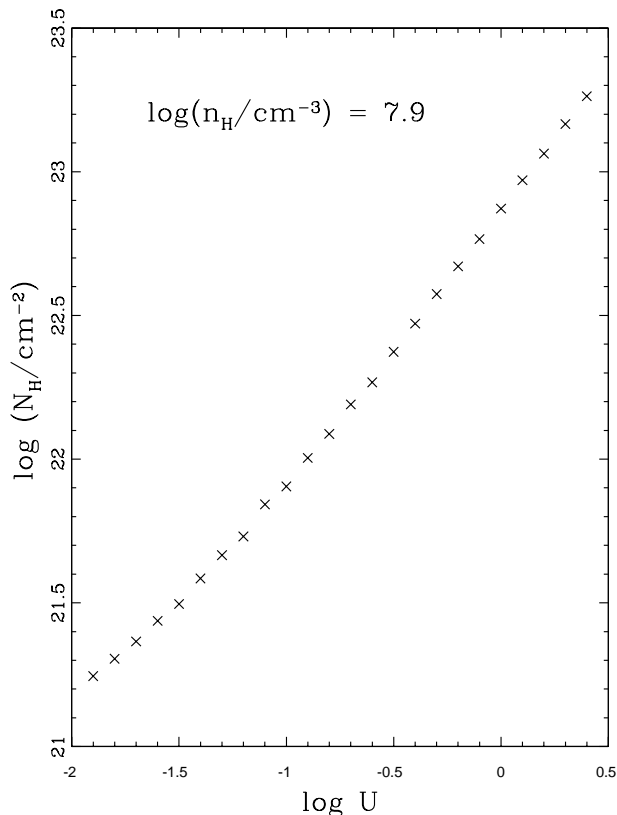


Figure 15. Plot of $\log N_{\text{H}}$ against $\log U$ at $\log(n_{\text{H}}/\text{cm}^{-3})=7.9$. Gridpoints are indicated by black crosses.

(2007). The values listed in Crenshaw & Kraemer (2012) for the ionization parameter ($\log U = -1.08$), radial distance (~ 0.1 pc) and mass outflow rate ($0.014 M_{\odot} \text{ yr}^{-1}$) found for the UV sub-component labelled 'D+Ec' lie within the range allowed in Fig. 14. Therefore the 2^3S state-helium absorber studied in this paper is consistent with the physical properties of 'D+E' without the high column density components labelled 'D+Ea' and 'Xhigh' contributing. The lack of high column absorbers in our study may not be totally surprising given the lack of detection of $H\beta$ absorption, in contrast to that found in the June 2000 HST observation reported in Crenshaw & Kraemer (2007). It is likely that our epoch 5 observations detect an outflow between the inner narrow line region and the BLR, possibly within an *intermediate line region* where self-absorption occurs (Crenshaw & Kraemer 2007). A hydrogen number density range of $7.1 \leq \log(n_{\text{H}}/\text{cm}^{-3}) \leq 8.8$ is intermediate to the BLR and NLR densities and is therefore consistent with the location found in the aforementioned papers. If this UV absorption results from the same obscurer as our epoch 5 observation, it rules out the crossing cloud scenario since, at the velocities listed in §5.3, the absorber would have completely crossed the emission region at least ~ 3 years before epoch 5.

Given the range of possible radial distances (see Fig. 14), the 2^3S helium epoch 5 absorber likely lies at or beyond the radial distance of the inner edge of the dusty torus. The torus is thought to surround the central regions

of AGN including NGC 4151, with a structure extending from the inner face out to a few pc (Riffel et al. 2009). In Koshida et al. (2014) the observed time lag between the V-band and K-band light-curve behaviour in NGC 4151 suggested an inner radius of the dust torus of approximately 30 to 80 lt-days. The earlier study of Minezaki et al. (2004) was consistent with this finding, having calculated a hot inner edge of the torus in NGC 4151 located at ≈ 0.04 pc from the central ionising source. It is therefore possible that the outflow consists of material originating in the torus, as has been proposed for a broad absorption line in Leighly et al. (2015).

6 SUMMARY

The results of this investigation can be summarised as follows:

- (i) The absorption due to He I $\lambda 20587$ has a similar profile to that at 10830 \AA , indicating that they originate in the same outflowing gas. Use of this line, which is not commonly examined in AGN studies, in combination with the triplet state transitions, provides useful constraints on the parameter space occupied by the outflow.
- (ii) The near-IR component of the triplet state helium absorber in epoch 5 is likely to be saturated over most of its velocity range, since the depth of the optical component is significantly stronger than that predicted by an absorption profile obtained by scaling down the optical depth of the near-IR component by a factor 23.3 based on the $f\lambda$ ratio.
- (iii) The continuum behaviour, together with the variability pattern across the observational epochs, suggests changes in the ionization state driven by a variable continuum are the cause of the observed variability of the epoch 5 absorber.
- (iv) The observed variability is consistent with changes in absorber covering fraction of the emission region. The absorber strength is consistent with zero, therefore being entirely outside the line-of-sight, at epochs 1 and 2. It would reach peak coverage near epoch 5 before moving out again prior to epoch 6. However, the lack of multiple significant absorber measurements precludes conclusive evidence of this mechanism.
- (v) Photoionization simulations are used to constrain the epoch 5 absorber properties. The total hydrogen number density and column density ranges are $7.1 \leq \log(n_{\text{H}}/\text{cm}^{-3}) \leq 8.8$ and $21.2 \leq \log(N_{\text{H}}/\text{cm}^{-2}) \leq 23.3$ respectively, while the ionization parameter range is $-1.9 \leq \log U \leq 0.4$. Ninety per cent of the gridpoints record radial distance from the continuum source of $0.03 \leq r \leq 0.49$ pc with a maximum permitted value of 1.1 pc.
- (vi) The epoch 5 absorber shows similarities to that arising from the absorber complex labelled 'D+E' in NGC 4151 reported in (Kraemer et al. 2005, 2006; Crenshaw & Kraemer 2007, 2012). The properties of the epoch 5 absorber are what would be expected if the highest column density components of 'D+E' were excluded. The lack of $H\beta$ absorption in our spectra suggests these high column components are indeed no longer present.
- (vii) The mass outflow rate due to the epoch 5 absorber is calculated to be between 0.008 and $0.38 M_{\odot} \text{ yr}^{-1}$. This outflow rate implies a contribution to the kinetic luminos-

ity which is low in comparison to the bolometric luminosity, therefore the outflow is not a significant contributor to feedback effects. Compared to the mass accretion rate, the possible mass outflow rate ranges from approximately 0.6 to 29 times as large.

ACKNOWLEDGEMENTS

We thank the anonymous referee for their helpful comments which led to the improvement of this paper. This work is supported at the University of Leicester by the Science and Technology Facilities Council (STFC). HL is supported by a European Union COFUND/Durham Junior Research Fellowship (under EU grant agreement number 267209).

REFERENCES

- Allende Prieto C., Lambert D. L., Asplund M., 2001, *ApJ*, 556, L63
- Allende Prieto C., Lambert D. L., Asplund M., 2002, *ApJ*, 573, L137
- Arav N., 1998, in Kaper L., Fullerton A. W., eds, *Cyclical Variability in Stellar Winds Outflows in Quasars: Radiative Acceleration and Variability*. p. 402
- Arav N., 2004, 311, 213
- Arav N., Becker R. H., Laurent-Muehleisen S. A., *et al.* 1999, *ApJ*, 524, 566
- Benjamin R. A., Skillman E. D., Smits D. P., 1999, *ApJ*, 514, 307
- Bentz M. C., Denney K. D., Cackett E. M., *et al.* 2006, *ApJ*, 651, 775
- Bray I., Burgess A., Fursa D. V., *et al.* 2000, *A&AS*, 146, 481
- Capellupo D. M., Hamann F., Barlow T. A., 2014, *MNRAS*, 444, 1893
- Capellupo D. M., Hamann F., Shields J. C., *et al.* 2013, *MNRAS*, 429, 1872
- Chelouche D., Netzer H., 2001, *MNRAS*, 326, 916
- Collin-Souffrin S., Dumont A. M., 1990, *A&A*, 229, 292
- Crenshaw D. M., Kraemer S. B., 2007, *ApJ*, 659, 250
- Crenshaw D. M., Kraemer S. B., 2012, *ApJ*, 753, 75
- Crenshaw D. M., Kraemer S. B., Hutchings J. B., *et al.* 2000, *ApJ*, 545, L27
- Crenshaw D. M., Kraemer S. B., Schmitt H. R., *et al.* 2009, *ApJ*, 698, 281
- Crenshaw D. M., Rodriguez-Pascual P. M., Penton S. V., *et al.* 1996, *ApJ*, 470, 322
- Cushing M. C., Vacca W. D., Rayner J. T., 2004, *PASP*, 116, 362
- Drake G. W., 1971, *Phys. Rev. A*, 3, 908
- Edelson R. A., Alexander T., Crenshaw D. M., *et al.* 1996, *ApJ*, 470, 364
- Everett J. E., 2005, *ApJ*, 631, 689
- Fabricant D., Cheimets P., Caldwell N., *et al.* 1998, *PASP*, 110, 79
- Ferland G. J., Porter R. L., van Hoof P. A. M., *et al.* 2013, *Rev. Mexicana Astron. Astrofis.*, 49, 137
- Filippenko A. V., 1982, *PASP*, 94, 715
- Filiz Ak N., Brandt W. N., Hall P. B., *et al.* 2013, *ApJ*, 777, 168
- Giustini M., Proga D., 2012, *ApJ*, 758, 70
- Gordon K. D., Clayton G. C., Misselt K. A., *et al.* 2003, *ApJ*, 594, 279
- Grandi S. A., 1982, *ApJ*, 255, 25
- Grevesse N., Sauval A. J., 1998, *Space Sci. Rev.*, 85, 161
- Guo D.-F., Hu S.-M., Tao J., Yin H.-X., Chen X., Pan H.-J., 2014, *Research in Astronomy and Astrophysics*, 14, 923
- Hamann F., Barlow T. A., Junkkarinen V., *et al.* 1997, *ApJ*, 478, 80
- Hamann F., Kaplan K. F., Rodríguez Hidalgo P., *et al.* 2008, *MNRAS*, 391, L39
- Holweger H., 2001, in Wimmer-Schweingruber R. F., ed., *Joint SOHO/ACE workshop "Solar and Galactic Composition"* Vol. 598 of American Institute of Physics Conference Series, Photospheric abundances: Problems, updates, implications. pp 23–30
- Hopkins P. F., Elvis M., 2010, *MNRAS*, 401, 7
- Hutchings J. B., Crenshaw D. M., Kaiser M. E., *et al.* 1998, *ApJ*, 492, L115
- Hutchings J. B., Crenshaw D. M., Kraemer S. B., *et al.* 2002, *AJ*, 124, 2543
- Iserlohe C., Krabbe A., Larkin J. E., *et al.* 2013, *A&A*, 556, A136
- Ji T., Zhou H., Jiang P., *et al.* 2015, *ApJ*, 800, 56
- Jin C., Ward M., Done C., *et al.* 2012, *MNRAS*, 420, 1825
- Kaspi S., Maoz D., Netzer H., *et al.* 2005, *ApJ*, 629, 61
- Kong M.-Z., Wu X.-B., Wang R., *et al.* 2006, *A&A*, 456, 473
- Korista K., Baldwin J., Ferland G., *et al.* 1997, *ApJS*, 108, 401
- Koshida S., Minezaki T., Yoshii Y., *et al.* 2014, *ApJ*, 788, 159
- Kraemer S. B., Crenshaw D. M., Gabel J. R., *et al.* 2006, *ApJS*, 167, 161
- Kraemer S. B., Crenshaw D. M., Hutchings J. B., *et al.* 2001, *ApJ*, 551, 671
- Kraemer S. B., George I. M., Crenshaw D. M., *et al.* 2005, *ApJ*, 633, 693
- Kriss G. A., Davidsen A. F., Zheng W., *et al.* 1999, *ApJ*, 527, 683
- Landt H., Bentz M. C., Ward M. J., *et al.* 2008, *ApJS*, 174, 282
- Landt H., Elvis M., Ward M. J., *et al.* 2011, *MNRAS*, 414, 218
- Leighly K. M., Cooper E., Grupe D., *et al.* 2015, *ApJ*, 809, L13
- Leighly K. M., Dietrich M., Barber S., 2011, *ApJ*, 728, 94
- Liu W.-J., Zhou H., Ji T., *et al.* 2015, *ApJS*, 217, 11
- Magorrian J., Tremaine S., Richstone D., *et al.* 1998, *AJ*, 115, 2285
- Minezaki T., Yoshii Y., Kobayashi Y., *et al.* 2004, *ApJ*, 600, L35
- Nardini E., Reeves J. N., Gofford J., *et al.* 2015, *Science*, 347, 860
- Osterbrock D. E., Ferland G. J., 2006, *Astrophysics of gaseous nebulae and active galactic nuclei*
- Peterson B. M., Wanders I., Bertram R., *et al.* 1998, *ApJ*, 501, 82
- Pigarov A. Y., Terry J. L., Lipschultz B., 1998, *Plasma Physics and Controlled Fusion*, 40, 2055
- Polletta M., Tajer M., Maraschi L., *et al.* 2007, *ApJ*, 663,

- 81
- Popović L. Č., 2003, ApJ, 599, 140
- Pounds K. A., King A. R., Page K. L., *et al.* 2003, MNRAS, 346, 1025
- Rayner J. T., Toomey D. W., Onaka P. M., *et al.* 2003, PASP, 115, 362
- Riffel R., Rodríguez-Ardila A., Pastoriza M. G., 2006, A&A, 457, 61
- Riffel R. A., Storchi-Bergmann T., McGregor P. J., 2009, ApJ, 698, 1767
- Risaliti G., 2010, in Peterson B. M., Somerville R. S., Storchi-Bergmann T., eds, IAU Symposium Vol. 267 of IAU Symposium, The Structure of AGNs from X-Ray Absorption Variability. pp 299–306
- Savage B. D., Sembach K. R., 1991, ApJ, 379, 245
- Scannapieco E., Oh S. P., 2004, ApJ, 608, 62
- Schnülle K., Pott J.-U., Rix H.-W., *et al.* 2013, A&A, 557, L13
- Shakura N. I., Sunyaev R. A., 1973, A&A, 24, 337
- Silk J., Rees M. J., 1998, A&A, 331, L1
- Smits D. P., 1996, MNRAS, 278, 683
- Véron-Cetty M.-P., Joly M., Véron P., 2004, A&A, 417, 515
- Wang J.-M., Chen Y.-M., Hu C., 2006, ApJ, 637, L85
- Wang T., Yang C., Wang H., *et al.* 2015, ApJ, 814, 150
- Wildy C., Goad M. R., Allen J. T., 2015, MNRAS, 448, 2397
- Wills B. J., Netzer H., Wills D., 1985, ApJ, 288, 94

This paper has been typeset from a $\mathrm{T}_{\mathrm{E}}\mathrm{X}$ / $\mathrm{L}^{\mathrm{A}}\mathrm{T}_{\mathrm{E}}\mathrm{X}$ file prepared by the author.